Nanoscale Horizons

The home for rapid reports of exceptional significance in nanoscience and nanotechnology

This article can be cited before page numbers have been issued, to do this please use: R. Kesarwani, M. Veverka, M. Žáek, J. Vejpravova, V. Varade, L. Fekete and M. Kalbac, *Nanoscale Horiz.*, 2025, DOI: 10.1039/D5NH00291E.

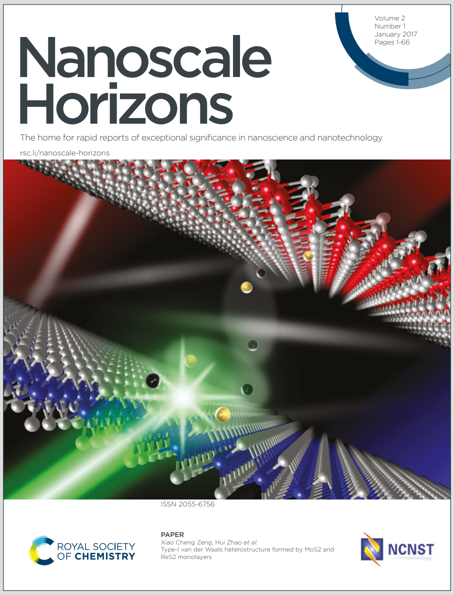

ROYAL SOCIETY OF CHEMISTRY

rsc.li/nanoscale-horizons

View Article Online
DOI: 10.1039/D5NH00291E

New concepts

We introduce a novel mechanochemical strategy—nanorolligami—for engineering optical anisotropy in monolayer MoS_2 by inducing controlled rolling through surface hydrophobization. This center-initiated, slow rolling process, moderated by flake tearing, enables scalable fabrication of uniform nanostructures with diameters of 100–200 nm. Unlike previous approaches relying on external fields or complex patterning, our method leverages surface chemistry to achieve precise control over nanoscale curvature and chiral morphology.

These rolled regions exhibit markedly enhanced chiroptical properties. Polarization-resolved photoluminescence measurements reveal circular and linear polarization ratios of up to 37% and 28%, respectively—substantially exceeding the ~8% observed in unrolled regions. This enhancement is driven by local field effects, interlayer scattering, and geometric confinement-induced optical resonances, offering a new pathway for modulating light–matter interactions in 2D systems.

This work establishes a new platform for tuning optical properties via structural reconfiguration and provides fundamental insight into symmetry breaking and chiral photophysics in van der Waals materials. The nanorolligami approach holds promise for a broad range of applications, including chiral light emitters, polarization-sensitive detectors, and enantioselective sensors, advancing next-generation nanophotonic and quantum technologies.

View Article Online
DOI: 10.1039/D5NH00291E

Unveiling Giant Polarisation Ratio of Chiral Photoluminescence in MoS_2 Nanorolligami Fabricated by Centre-to-Edge Rolling Mechanism

Rahul Kesarwani[1, 2], Miroslav Veverka[1], Martin Žáček[1], Vaibhav Varade[1], Ladislav Fekete[3], Martin Kalbac[2], and Jana Vejpravova[1]*

[1] Department of Condensed Matter Physics, Faculty of Mathematics and Physics, Charles University, Ke Karlovu 5, 121 16 Prague 2, Czech Republic

[2] Department of Low-Dimensional Systems, J. Heyrovsky Institute of Physical Chemistry, Dolejskova 3, 182 23 Prague 8, Czech Republic

[3] Department of Analysis of Functional Materials, Institute of Physics of the Czech Academic of Sciences, Na Slovance 2, 182 00 Prague 8, Czech Republic

*Email: jana.vejpravova@matfyz.cuni.cz

Keywords: Photoluminescence, Raman Spectroscopy, Light-matter Interaction, Circular Polarisation, Transition Metal Dichalcogenides, Nanorolligami, Optical Anisotropy

Abstract

We introduced mechanical strain to systematically roll monolayer (1-L) MoS_2 into nanostructures with diameters ranging from 100 – 200 nm. The rolled MoS_2 regions exhibit unique anisotropic optical behaviour compared to the flat regions (thickness $\leq$ 1 nm), as analysed through polarisation-resolved photoluminescence (PL) and Raman spectroscopy. Raman spectroscopy revealed that the E_{2g}/A_{1g} intensity ratio under circular polarisation was approximately 0.25 in the rolled regions, whereas it approached zero in the flat region. These findings highlight pronounced optical anisotropy and symmetry-breaking in rolled MoS_2, distinguishing it from the isotropic flat regions. Additionally, angular-dependent PL measurements demonstrated a strongly enhanced linear polarisation ratio (LPR) of 28% and circular polarisation ratio (CPR) of 37% in the rolled regions, indicating strong optical anisotropy. In contrast, the flat MoS_2 regions exhibited isotropic behaviour, with LPR and CPR values typically around 8%. Our results demonstrate that rolling-induced localised deformation profoundly modifies exciton polarisation behaviour in MoS_2. Enabling precise light filtering and nanoscale manipulation via nanoscrolling of the two-dimensional materials, our work lays the foundation for next-generation optoelectronic devices with tailored optical responses and enhanced functionality.

View Article Online
DOI: 10.1039/D5NH00291E

Introduction

Two-dimensional (2D) transition metal dichalcogenides (TMDs) have demonstrated the potential to revolutionise the field of nanotechnology due to their exceptional electronic, optical, and mechanical properties[1,2]. Recent efforts to enhance their performance – primarily through sophisticated exploitation of unique light-matter interactions – have involved their transformation from flatness to various layered[3,4] and confined structures[5,6].

Among these architectures, micro- to nanoscrolls of TMDs have recently emerged as highly promising variants, benefiting from the mesoscopic corrugation of the original TMD monolayer (1-L). This modification enhances the material's anisotropy and opens new possibilities for diverse applications[7–10]. Notably, this transformation retains the high surface area characteristic of 1-L counterparts while introducing distinct optical, electronic, and mechanical characteristics[9–12].

Generally, the rolling process induces mirror symmetry breaking, similarly to that observed in carbon nanotubes (CNTs)[13]. However, its impact is expected to be less pronounced due to the diameter differences between the typical TMD-based scroll (ranging from micrometres to several tens of nanometres) and CNTs. Nevertheless, mesoscopic corrugation may still enhance key physical properties, such as photoluminescence (PL) and charge transport[9,14].

The most striking effects of rolling can be observed in the optical response. In multilayer TMDs, strong interlayer coupling and defects typically reduce the intensity of PL[15]. However, in the artificially rolled architectures, the absence of such strong interlayer coupling allows each layer to contribute independently to the overall PL intensity[14,16], making these rolled structures highly suitable for advanced and optoelectronic photonics applications[9,17–19].

Thus, nanoscrolls have the potential to amplify the photon absorption cross-section, thereby enhancing light absorption efficiency. Furthermore, shape anisotropy can selectively enhance the emission of certain polarised light components compared to 1-L TMDs [17,18,20,21]. In addition, recent work has demonstrated that MoS_2 nanoparticles can exhibit enhanced photothermal effects under visible laser excitation due to efficient light trapping and anisotropic absorption, which could be further amplified in rolled geometries illuminated by circularly polarized light[22].

Another interesting consequence of rolling is the local field effect, which is particularly advantageous in optoelectronic devices requiring strong and controllable light emission[23]. Additionally, the nanorolling of TMDs influences the photogenerated current by minimising internal scattering and recombination losses – critical factors for applications in photodetectors and solar cells [9,10,12,17,18].

Recently discovered Janus-type narrow nanoscrolls have demonstrated the potential to enhance the rolling effect by introducing intrinsic out-of-plane built-in electric fields due to the different chalcogens within the rolled layer. However, strong interlayer interactions have been reported in these tubular structures [24,25].

Although the rolled TMD-based architectures offer numerous promising applications, in particular in optoelectronics and photonics, the absence of a reliable method for the large-scale fabrication of smoothly rolled flakes limits the broader utilisation of nanoscrolls in these emerging concepts.

Furthermore, the valley-related physics inherent to TMDs positions the interaction of chiral light with these materials as a fundamental aspect in optically-driven valleytronics and other applications that harness chiral and non-trivial light. However, despite its profound implications, this avenue remains largely unexplored in the scrolled TMD-based architectures[26–28].

In this work, we introduce a robust fabrication method yielding regular nanoscrolls of 1-L MoS_2 on a SiO_2/Si substrate, formed through symmetric centre-to-edge rolling. We successfully prepared rolled structures with varying thicknesses ranging from 100 nm to 200 nm.

Following a thorough state-of-the-art characterisation, we employed polarisation-resolved Raman and PL microspectroscopy to investigate the impact of the scroll-type topographic variation in comparison to the response of the flat regions (thickness $\leq$ 1 nm) of the same sample. Our experiments revealed striking differences in PL and Raman mode intensities between the flat and rolled regions, particularly under illumination with circularly polarised light.

While the PL experiments using linearly polarised light confirmed the expected behaviour, featuring anisotropy and an overall enhancement of the PL compared to the flat regions, dichroic experiments using right circularly polarised (RCP) and left circularly polarised (LCP) light exhibited approximately a 50% difference in PL intensities between the two emission channels.

View Article Online
DOI: 10.1039/D5NH00291E

The pronounced chiral light-matter interaction observed in these nanostructures underscores its growing importance for a wide range of modern applications, from quantum information technologies to next-generation photonic and optoelectronic devices.

Results and Discussion

First, the 1-L TMD flakes were synthesised on an SiO_2/Si substrate (300 nm) via chemical vapour deposition CVD at elevated temperatures (further details in Methods). Next, the rolling process was induced by dropping a 2:1 mixture of water and ethanol on top of the substrate containing the grown flakes, which were regularly distributed over the substrate area. However, different resulting architectures were observed depending on the post-treatment of the substrate with the grown 1-L MoS_2 flakes.

Our observations contrast somewhat with previous studies, where the rolling mechanism is expected to be strain-driven, and the formation of the rolls occurs rapidly. It is worth noting that during the cooling phase of the CVD process, strain is typically induced within the TMD flakes due to the mismatch in the thermal expansion coefficients between the TMD flakes and the substrate. The accumulated strain facilitates roll formation when a polar mixed ethanol-water solution is applied to the surface. The solution is expected to penetrate beneath the MoS_2 layer from the edge of the flake. Once the edge lifts, the roll forms quickly[7].

In our case, rapid edge-initiated rolling and almost identical final topography were achieved when using a freshly prepared sample. However, we discovered that if the sample is aged, the rolling mechanism is completely different due to the surface hydrophobisation.

The formation of TMD nanorolligami was captured using a charged-coupled device (CCD) camera attached to an optical microscope (OM), as shown in Movie M1 – M3 in the Supplementary Information (SI), which respectively show rolling behavior in aged, styrene-exposed (24 hr), and freshly prepared 1-L MoS_2 samples under a 2:1 water–ethanol solution. A schematic illustration of the observed mechanism of the nanorolligami formation is shown in Figure 1.

In contrast to the rolling behaviour of fresh samples, aged samples exhibited uniform rolling, resulting in smooth, crack-free nanoscrolls. We tentatively attribute this difference in rolling to the presence of a small amount of non-polar hydrocarbon molecules deposited onto the MoS_2 surface from the environment. We assume that hydrocarbons preferentially adhere to the edges of MoS_2 flakes rather than the central regions, where a small amount of MoO_x is typically present near the nucleation centre of the grown flake[29]. In such a case, the polar solvent is

View Article Online
DOI: 10.1039/D5NH00291E

repelled from the edges and instead penetrates beneath the MoS_2 layer in the MoO_x-rich central part of the flake.

To support our hypothesis and confirm the crucial role of hydrocarbons in altering the rolling mechanism, the as-deposited MoS_2 sample was exposed to styrene vapour under atmospheric pressure for 24 hours, followed by the same rolling procedure using an ethanol-water solution. The rolling behaviour of the styrene-exposed sample closely resembled that of the aged samples, with rolling initiated uniformly from each corner. Conversely, the as-deposited sample (of the same age) exhibited high roughness and random crumpling after solution exposure, as evident from the optical images (Figure S1) and AFM analysis (Figure S2) in the SI. Notably, the AFM height profiles (positions P1–P4) confirm that the styrene-exposed MoS_2 maintains intact 1-L regions between the rolled edges, while the as-deposited sample shows irregular folding and increased surface deformation. Furthermore, unlike the edge-rolling mechanism, the centre-to-edge process involves the tearing of 1-L MoS_2, which significantly slows down the rolling. This deceleration is crucial, as we believe it facilitates the formation of rolls with greater uniformity and smoother rolling behaviour, ultimately enhancing the overall process quality.

As a next step, the morphology and height (thickness) of the nanorolligami structures that slowly rolled via the centre-to-edge mechanism were inspected using AFM. Figure 2a presents the AFM image of a representative, fully scrolled 1-L MoS_2. Optical images captured at larger scale (Figure S3a in the SI) demonstrate the consistent formation of this rolling pattern in other parts of the sample. Since the rolled regions are located at the edges of the original flat MoS_2 flake, it is evident that the 1-L MoS_2 breaks from the centre and rolls up at the edges.

Further investigation of surface morphology focused on evaluating height uniformity, plateau shapes, and rolling types. For clarity, we defined three distinct regions on the sample – R1, R2, and R3 – and measured the height profiles at arbitrary points within each region to compare their thicknesses. Region R1 represents the unrolled part, resembling a flat or 1-L MoS_2, while regions R2 and R3 correspond to the rolled parts of the architecture.

Figure 2b provides an enlarged view of the R1 region. We determined the corresponding height profiles at selected positions (P1 – P3). The average thickness across these positions is approximately 1 nm, signifying the typical thickness of a 1-L MoS_2.

The magnified images of regions R2 and R3 are shown in Figure 2c and Figure 2d, respectively, where we similarly selected three positions and determined the height profiles. The measured

View Article Online
DOI: 10.1039/D5NH00291E

thicknesses at these positions were approximately 200 nm and 180 nm for the R2 and R3, respectively. However, across the entire arm of R2 and R3, the nanoscroll thickness varied within a range of 110 – 220 nm and 100 – 200 nm, as shown in SI, Figure S3b.

Assuming a perfect roll with a rolled area length of approximately 5 µm, a spiral turn thickness of 1 nm, and an outer diameter of about 150 nm, the inner diameter of the roll was estimated to be 126 nm, resulting in approximately 12 shells. Based on these observations, we speculate that the plateau in the rolling of R2 exhibits a ridge-like structure, while R3 presents a butte-like morphology. The lower-height regions within the rolled portions of R2 and R3 display surfaces resembling eroded ridges. This morphological variation may stem from uneven or insufficient intercalation of the ethanol-water solution, which likely led to incomplete strain relaxation. Areas with lower intercalation may have experienced varying degrees of rolling, with slower rolling in regions where the strain was not fully minimised. Consequently, the surfaces in these regions appear as ridge-like or eroded features.

Nevertheless, the vast majority of the flake is smoothly rolled, with the same type of structure forming consistently across the substrate. Thus, the availability of the regularly rolled 1-L MoS_2 provides a unique opportunity to investigate light-matter interactions in concentrically curved 1-L MoS_2 surfaces, using both linearly and circularly polarised light.

For these experiments, we captured PL spectral map at 300 K, as shown in SI, Figure S4, which reveal higher PL intensity in rolled regions compared to 1-L areas, along with a marked dependence on the polarization state. For the single-point optical spectra (in Figure 3a–d), data were extracted from specific positions on both the 1-L and rolled regions of the mapped nanorolligami. The following notation was used: horizontal and vertical linear polarisations are labelled as X and Y, respectively, while right and left circular polarisations are labelled as σ^+ and σ^-. The full description of the polarisation settings for the experiment specifies both the incident polarisation and the analyser setting (e.g., XX indicates that horizontal polarisation was set for both the incident light and the analyser).

The in-plane polarisation orientation (X and Y) was not explicitly calibrated with respect to the roll axis. However, the polarisation states were determined based on the angular dependence observed in the polar plots of the Raman/PL intensities, ensuring consistent alignment during measurements. Figure 3a and 3b present the normalised PL spectra of the rolled and flat MoS_2 regions for the linear and circular co-polarisations (where the incident and detected light are in the same polarisation state), respectively.

View Article Online
DOI: 10.1039/D5NH00291E

In the PL spectra measured under linear polarisation (Figure 3a), the flat 1-L MoS_2 region exhibits strong A-excitons at 1.821 eV and weak B-excitons at 1.961 eV, with no observed shift in peak positions between the XX and YY polarisation states. In contrast, the rolled MoS_2 region shows A-excitons at 1.847 eV and 1.862 eV for XX and YY co-polarisations, respectively, with no B-exciton resolved. The shift in the A-exciton peak positions between the flat and rolled MoS_2 is 26 meV for XX and 41 meV for YY, respectively. The 15 meV difference between the XX and YY polarisation states in the rolled region could be attributed to the curvature-induced symmetry reduction, which modifies the electronic band structure and excitonic transitions[30–33].

Similarly, in the PL spectra of the flat MoS_2 measured with circularly polarised light (Figure 3b), the A-excitons appear at nearly identical positions: 1.806 eV and 1.809 eV for the $\sigma^+\sigma^+$ and $\sigma^-\sigma^-$ states, respectively, with a weak B-exciton observed at 1.953 eV (no difference between $\sigma^+\sigma^+$ and $\sigma^-\sigma^-$ co-polarisations). In contrast, the rolled MoS_2 region shows A-exciton peaks at 1.837 eV and 1.856 eV for the $\sigma^+\sigma^+$ and $\sigma^-\sigma^-$ co-polarisations, respectively, with no B-exciton resolved. The observed shift between the flat and rolled regions is 31 meV for $\sigma^+\sigma^+$ and 47 meV for $\sigma^-\sigma^-$, while the 19 meV difference between the $\sigma^+\sigma^+$ and $\sigma^-\sigma^-$ states in the rolled region is similarly attributed to curvature-induced symmetry reduction[30–32].

The shift due to the quantisation effect can be estimated using the formula[34]:

$$\Delta E_g = \frac{\pi^2 \hbar^2}{\mu L_z^2} \tag{1}$$

where ΔE_g is the change in the band gap energy, $\hbar$ is Planck's constant, μ is the effective exciton mass in the direction parallel to the c-axis ($\mu = (m_e \times m_h)/(m_e + m_h)$, where m_e and m_h represent the effective masses of electrons and holes, respectively[35].), and L_z is the thickness along c-axis (number of shells ≈ 12 × interlayer distance in MoS_2 ≈ 0.615 nm = 7.38 nm). The expected shift is approximately 16 meV, which is in very good agreement with the experimental results.

Figure 3e presents the ratios of PL intensities (total area under the curve) for experiments using the circular ($\sigma^+\sigma^+/\sigma^-\sigma^-$) and linear ($XX/YY$) co-polarisations for the rolled and flat MoS_2, respectively. For the rolled MoS_2 region, the PL intensity ratio (XX/YY) is significantly higher (~2.4) compared to that of the flat region (~1.3). A similar trend was observed at different positions for the circular co-polarisation, with consistently higher PL intensity ratios in the rolled regions compared to the flat MoS_2, indicating enhanced polarization sensitivity (for more details, see SI, Figure S5).

View Article Online
DOI: 10.1039/D5NH00291E

The false-colour map in Figure 3g illustrates the polarisation contrast for the MoS_2 sample, which includes both rolled and flat regions. The difference between the PL intensities measured under right circular polarisation ($\sigma^+\sigma^+$) and left circular polarisation ($\sigma^-\sigma^-$) was plotted. As observed, the difference is significantly greater in the rolled regions compared to the flat MoS_2 region. This indicates that the polarisation effect is much more pronounced in the rolled regions when switching the incident light polarisation from σ^+ to σ^-. The observed difference can be attributed to curvature-induced symmetry reduction in the rolled regions, as explained earlier, arising from momentum quantisation around the circumference and changes in the orbital composition of the Bloch band[31,32].

The PL mapping of rolled MoS_2 under both circular and linear cross-polarised light, along with the PL intensity ratios estimated at four different positions, reveal consistently higher PL intensity in the rolled regions compared to the flat MoS_2. Although the contrast in intensity ratios is slightly reduced compared to co-polarised cases, the results still confirm anisotropic optical responses induced by the rolling process (see SI, Figure S6 and Figure S7 for details).

The observed increase in the PL intensity of the nanoscroll can be attributed to the following mechanisms:

1. **Cumulative scattering of photo-generated photons within each layer of MoS_2.** Since the rolled region consists of multiple uncoupled layers (as confirmed by the absence of interlayer coupling peaks in PL and the lack of low-frequency modes in Raman spectra – see in SI, Figure S8), each layer contributes to an overall increase in the PL intensity[36–38].

2. **Strong photon field interactions.** The photon field (local field) generated by the bottom layers interacts with the top rolling layer, which remains independent of the bottom layers. This interaction enhances the PL intensity of the top rolling layer, similar to how near-field intensity increases in the presence of local fields generated by nanoparticles. As a result, the overall PL intensity of the rolled MoS_2 is significantly higher than that of the flat 1-L MoS_2 region[23,39].

3. **Formation of whispering gallery modes.** In the MoS_2 nanoscroll, two waves propagating in opposite directions form standing waves, known as whispering gallery modes, enable the tubes to function as effective optical resonators[40].

To further validate the scenario behind the strong PL enhancement and the giant degree of polarisation of CP light, PL measurements were conducted using unpolarised incident light, detecting σ^+ and σ^- components (which can be interpreted as two perpendicular, linearly polarised components) and vice versa (Figure S9 in SI). Identical PL intensity was observed for both flat and rolled regions under these conditions, confirming that the PL intensity difference observed in Figure 3a and 3b (for $\sigma^+\sigma^+$ and $\sigma^-\sigma^-$ configurations, respectively) is neither due to valley polarisation enhancement nor to the simple superposition of signals from individual layers. Instead, these complementary experiments support the scenario of anisotropic light confinement within the MoS_2 nanoscroll[41].

Similar enhancements in Raman intensity were observed under both co- and cross-polarisation conditions, with the A_{1g} and E_{2g} modes exhibiting distinct activation patterns in the rolled and flat regions. The full Raman maps and polarization-dependent trends are presented in SI, Figures S10 and Figure S11.

Figure 3c presents the normalised Raman spectra for both rolled and flat MoS_2 regions obtained using the linear co-polarisation setup (*XX* and *YY*). From the analysis of the spectra, we found that both E_{2g} and A_{1g} modes are activated both in the rolled and flat MoS_2 regions. Additionally, a ~1 cm^{-1} shift in the circular co-polarisation spectra between the rolled and flat regions can be attributed to residual strain induced by the rolling process.

Figure 3d illustrates the normalised Raman spectra for the rolled and flat MoS_2 regions under circular co-polarisation ($\sigma^+\sigma^+$ and $\sigma^-\sigma^-$). In the case of the flat MoS_2, only the A_{1g} mode is active, which aligns with the literature[42]. However, in the rolled MoS_2, both E_{2g} and A_{1g} modes are activated. This observation can be explained by the continuous change in the mutual orientation between the MoS_2 plane and the direction of incident/measured light, which will be discussed later in this section.

Now, let us consider the full width at half maximum (FWHM) and intensities of both E_{2g} and A_{1g} modes. These parameters are found to be higher for the flat MoS_2 region compared to the rolled MoS_2 region in both linear and circular co-polarisation. This difference can be attributed to variations in the interaction between the laser beam and the sample surface. Specifically, the area of the sample irradiated by the incident light significantly influences the resulting spectra. Assuming a circular beam with a diameter of ~1 μm, the irradiated area of flat MoS_2 would be approximately 0.75 μm^2. In contrast, for the rolled MoS_2, only 0.15 μm^2 of the rolled area (assuming a diameter of ~0.15 μm) would be irradiated. This estimation suggests that the intensity of the spectra from the flat region should be about five times stronger than that of the rolled region.

View Article Online
DOI: 10.1039/D5NH00291E

However, in the case of the rolled MoS_2, additional layers within the scroll likely contribute to scattered light. In experiments using linearly polarised light, the intensity of the rolled region was observed to be roughly twice that of the flat region, suggesting that, effectively, 2.5 layers of the MoS_2 nanoscroll contribute to the Raman spectrum. Given that a single MoS_2 layer absorbs approximately 10% of the light intensity, one would expect that around 10 layers to contribute to the emission. Ideally, this would enhance the spectra by a factor of 10. Additionally, for the flat MoS_2 sample on a SiO_2/Si substrate, Raman spectra are enhanced due to interference effects, a phenomenon not expected in the case of rolled MoS_2. Accounting for all these factors, it appears that interference effects increase the signal from the flat sample by a factor of 4.

Moreover, we estimated the E_{2g}/A_{1g} intensity ratio for both circular and linear co-polarisation states in rolled and flat MoS_2, as shown in Figure 3f. The intensity ratio analysis revealed that under linear co-polarisation, the ratio remains similar for both rolled and flat MoS_2 (approximately 0.45), indicating comparable contributions from the in-plane (E_{2g}) and out-of-plane (A_{1g}) vibrational modes.

However, under circular co-polarisation, the behaviour diverges significantly. In the flat MoS_2 region, the ratio approaches zero, meaning only the out-of-plane mode is active, with the in-plane mode is almost entirely suppressed. This suppression is expected for 1-L MoS_2, due to symmetry selection rules under circular polarisation. In contrast, for the nanoscroll, the ratio remains around 0.25, indicating that both in-plane and out-of-plane modes are active under circular polarisation. This phenomenon occurs because the rolling process alters the orientation of the MoS_2 plane, allowing the in-plane mode to become active under circular polarisation, which is typically not observed in flat 1-L structures. These orientational changes are induced by the rolling relax the polarisation selection rules, thereby activating both vibrational modes[43,44].

Figure 3h presents a false-colour map showing the difference in intensity in A_{1g} mode intensity under $\sigma^+\sigma^+$ and $\sigma^-\sigma^-$ polarisation states for both rolled and flat 1-L MoS_2. As expected, the difference is significantly larger in the rolled MoS_2 region compared to the 1-L MoS_2 region, where the difference is minimal. The rolling process induces curvature and associated strain, which can locally distort the lattice structure and modify the electronic band structure. These changes lead to symmetry reduction, altering Raman selection rules in localised regions. While these distortions do not globally affect selection rules at the Γ-point, curvature and strain at

View Article Online
DOI: 10.1039/D5NH00291E

specific regions (e.g., edges or crumpled areas) may still contribute to the observed polarisation sensitivity of the A_{1g} Raman mode. This observation is consistent with tight-binding model theoretical insights[31].

Finally, the angular dependence of the PL and Raman spectra under the linear and circular co-polarisations was explored to examine optical and vibrational anisotropy. Angular-dependent measurements for rolled and flat regions were performed in locations close to those used for PL and Raman data (as shown in Figure 3), ensuring consistency across all measurements. Additional PL polar plots for two distinct positions are provided in SI (Figure S12). These measurements further support the presence of optical anisotropy introduced by the rolling process.

Figure 4a–d present normalised angular-dependent polar plots of the PL emission from the rolled MoS_2 sample under polarised light (X, Y, σ^+, and σ^-). The black circles represent the experimental data, while the red solid lines depict the fits using the equation:

$$r = A \times \left(1 + \rho \times cos\left(2[\theta - \phi]\right)\right) \tag{2}$$

where A is a normalisation constant, ρ is the polarisation ratio, θ is the angle of detection, and ϕ is the polarisation angle[45]. These angles refer to in-plane angles in the optical measurement setup, used for fitting angular-dependent intensity plots. This fitting approach allows us to estimate the linear polarisation ratio (LPR) and circular polarisation ratio (CPR), along with quantifying the PL anisotropy.

The estimated LPR values for X and Y polarised light are 27.3% and 28.5%, respectively, while the CPR values for σ^+ and σ^- polarised light are 37.6% and 35.1%, respectively. These results highlight that the rolling region exhibits a significantly higher degree of polarisation and anisotropy for circularly polarised light compared to linear polarised light – a phenomenon that will be discussed in detail later.

Interestingly, in the rolled region, the angular orientation of the PL intensity maxima, represented by the polarisation angle (ϕ), is nearly identical for both X and σ^+ polarised incident light, with values of ϕ = 0.3° for X and ϕ = 0.35° for σ^+ polarisation. A similar correlation is observed between Y and σ^- polarised light, with ϕ = 1.85° for Y and ϕ =1.9° for σ^- polarisation. This difference suggests that the observed PL intensity is modulated by the polarisation of the incident light, with contributions from the lower layers of the rolled structure adding to the top layer's emission. The rolling-induced anisotropy likely influences the emitted PL, leading to consistent angular orientations in the polarisation-dependent PL intensity. This interplay could explain the higher ρ and directional polarisation observed in the rolled region.

Similarly, Figure 4e–h present angular-dependent polar plots for the flat MoS_2 region under the same polarisation states. The fitting process yields an LPR of 8.2% and 8.4% for X and Y polarised light, and a CPR of 7.8% and 9% for σ^+ and σ^- polarised light, respectively. In contrast to the rolled region, the flat MoS_2 region displays almost isotropic behaviour, as evidenced by the much lower ρ across all polarisation states.

The rolling process introduces overall structural and optical anisotropy, as evidenced by the angular dependencies of PL and Raman spectra. These distortions modify exciton dynamics by altering the electronic environment and orbital composition of Bloch bands, as suggested by tight-binding models[31]. Unlike pristine 1-L MoS_2, where exciton coherence exceeds the recombination time, the rolled region exhibits a pronounced dependence on the incident polarisation, resulting in enhanced polarisation anisotropy.

The rolling-induced modifications, including curvature and local deformation, create regions with varying symmetry and selection rules, influencing the polarisation response[45–47]. Tight-binding theory suggests that curvature and momentum quantisation can alter excitonic behaviour by modifying symmetry locally. However, the observed spectra represent an average response over the laser spot size (~1 μm), incorporating contributions from both locally deformed and relatively undistorted regions. While these local distortions may not reduce symmetry globally, they can alter selection rules in specific regions, contributing to the unique polarisation response observed in the rolled region. This interplay of factors distinguishes the polarisation properties of the rolled region distinct from those of flat MoS_2.

Figure 5a–d presents the polar plots of the A_{1g} and E_{2g} modes in the rolled region under different incident light polarisations: X, Y, σ^+, and σ^-.

In Figure 5a, the polar plot for X-polarised light displays elliptical intensity variations with respect to the analyser angle for both the A_{1g} and E_{2g} modes. These phonon modes exhibit similar polarisability strengths along their respective directions. The physical interpretation of this behaviour can be linked to differences in how light interacts with the rolled 1-L MoS_2, potentially influenced by phonon anisotropy and localised strain effects, as discussed in prior studies[18,31–33,43–45].

View Article Online
DOI: 10.1039/D5NH00291E

Similarly, Figure 5b presents the polar plot for *Y*-polarised light. The elliptical shape of both A_{1g} and E_{2g} modes under *Y* polarisation closely mirrors the behaviour observed under *X* polarisation, indicating consistent anisotropic phonon behaviour in the rolling region under linear co-polarisation.

Figure 5c and Figure 5d display the polar plots for σ^+ and σ^- polarised light, revealing open dumbbell-shaped intensity distribution for both A_{1g} and E_{2g} modes. These shapes highlight the sensitivity of the rolled region to the handedness of circularly polarised light, likely stemming from localised curved strain, defects, or directional anisotropies induced by the rolling process[18,43–45].

The angular offset observed between the A_{1g} and E_{2g} modes may simply reflect differences in their respective phonon symmetries, as A_{1g} corresponds to out-of-plane vibrations, while E_{2g} corresponds to in-plane vibrations, meaning they interact differently with the polarised light. However, changes in intensity alone do not necessarily indicate symmetry lowering but may instead result from a combination of localised effects and directional superposition of polarisation states. Further investigations are required to precisely determine the origins of the observed angular dependencies.

In contrast, the polar plots for the flat MoS_2 region, presented in Figure 5e–h, demonstrate distinctly different behaviour compared to the rolled region. Under linear polarised light (*X* and *Y)*, the E_{2g} mode exhibits an almost circular (isotropic) polar plot in Figure 5e and Figure 5f, while the A_{1g} mode forms a dumbbell-shaped polar plot. This difference indicates that the 1-L MoS_2 retains its in-plane symmetry, with no significant strain-induced anisotropy affecting the E_{2g} mode. However, the dumbbell shape of the A_{1g} mode may indicate sensitivity to out-of-plane forces or interactions with the substrate[48]. The consistency of these shapes under *X* and *Y* light confirms the preserved hexagonal symmetry of the 1-L MoS_2.

For σ^+ and σ^-, Figure 5g and Figure 5h show closed, perpendicular dumbbell shapes for both the A_{1g} and E_{2g} modes in the 1-L region. This behaviour contrasts with the rolled region and suggests that σ^+ and σ^- light in 1-L MoS_2 interacts uniformly with the crystal's inherent phonon modes. The angular dependence in these plots aligns with the expected behaviour of 1-L MoS_2, as supported by existing literature[49,50]. Additional Raman polar plots for two distinct positions are included in the SI (Figure S13). These results further demonstrate the anisotropic vibrational response induced by the rolling process.

View Article Online
DOI: 10.1039/D5NH00291E

Now, let us examine the origin of the striking differences between the angular dependencies of the flat and rolled regions. Generally, for 1-L MoS_2 under circular polarised light (σ^+ and σ^-), only the in-plane A_{1g} mode remains active, as seen in Figure 3. However, under linear polarised light, both E_{2g} and A_{1g} modes appear. This behaviour changes in the rolled MoS_2 region, where both E_{2g} and A_{1g} modes can be observed, even with σ^+ and σ^- light.

To explain these observations, we calculated the Raman intensity for both the D_{6h} (6/*mmm*) point group, representing bulk 2H-MoS_2, and C_{3v} (3*m*) point group, representing bulk 3R-MoS_2. These calculations were performed for different incident light polarisations (σ^+, σ^-, *X*, and *Y*) by varying the detection (or analyser) angle. The full calculations and compiled Raman tensor values for both point groups are provided in the SI (see Note 1**)**.

In the manuscript, we specifically present the D_{6h} (6/*mmm*) point group at various ψ' orientations, as shown in Figure 6. This figure illustrates the interaction between laser light and the rolling surface. The laser beam, approximately 1 µm in diameter, interacts with the rolled surface (0.3 µm in diameter or less) at different positions and angles, resulting in variations in Euler angle values. As such, the recorded Raman signal may partially include contributions from both rolled and adjacent flat regions (could be substrate or MoS_2), leading to an averaged response. This spatial averaging can slightly reduce the modulation contrast in the angular-dependent Raman plots. Nevertheless, the observed anisotropic patterns are robust and consistent, indicating dominant contributions from the rolled structures. As the Euler angle ψ' varies, the Raman tensor values of MoS_2 also change, as referenced in the Bilbao Crystallography database[51–53]. We focus on Euler angle ψ' in this figure, as the rolling occurs in the *XZ* plane, causing only ψ' to change. It is noted that the ψ' an out-of-plane lattice orientation angle, used in theoretical symmetry-based modeling. For other orientations (θ' and ϕ'), we also calculated the Raman tensor for both D_{6h} and C_{3v} point groups, which is included in the **SI** (Note 1).

Table 1 presents the variation of the Euler angle ψ' for the out-of-plane Raman mode E_{2g} of the 2H phase of MoS_2 (D_{6h} point group) under different polarisations of light. The equations in the table describe the angular-dependent behaviour of the Raman mode for both circularly and linearly polarised light. Further discussions and derivations are provided in the SI (Note 1).

View Article Online
DOI: 10.1039/D5NH00291E

Table 1: Variation of the E_{2g} Raman mode intensity for 2H-MoS_2 (D_{6h} point group) as a function of the Euler angle ψ' under different polarization states.

D_{6h} (6/*mmm*) for bulk -2H MoS_2		Out of plane Raman mode (E_{2g}) by rotation of Euler angle ψ' (º)			
Equations at different polarization states in the θ angular rotation for Raman tensor{{a,*b*,*c*},{d,*e*,*f*},{*ii*,*jj*,*k*}}	Co-polarization state ($\theta = 0$)	0 {{*d′*,*0*,*0*},{0,-*d′*,*0*},{0,*0*,*0*}}	30 {{*r′*,0,*0*},{0,*s*,*k′*},{0,*k′*,*l*}}	60 {{*h′*,*0*,*0*},{0,*r′*,*s*},{0,*s*,*k′*}}	90 {{*e′*,*0*,*0*},{0,*0*,*0*},{0,*0*,*d′*}}
$I_{rcp-\theta}$ $\propto \frac{1}{4}[((c$ $+ sin\theta)$ $+ (cos\theta$ $- sin\theta)$ $+((cos\theta$ $+ sin\theta)$ $+ (sin\theta$ $- cos\theta)$	$I_{\sigma^+\sigma^+}$	$\equiv 0$	$\equiv (r'+s')^2$	$\equiv (h'+r')^2$	$\equiv (e')^2$
$I_{lcp-\theta}$ $\propto \frac{1}{4}[((c$ $+ sin\theta)$ $+ (cos\theta$ $- sin\theta)$ $+((sin\theta$ $- cos\theta)$ $+ (cos\theta$ $+ sin\theta)$	$I_{\sigma^-\sigma^-}$	$\equiv 0$	$\equiv (r'+s')^2$	$\equiv (h'+r')^2$	$\equiv (e')^2$
$I_{H-\theta}$ $\propto [a^2co$ $+ d^2sin$	$I_{XX} \propto a^2$	d'^2	r'^2	h'^2	e'^2
$I_{V-\theta}$ $\propto [e^2co$ $+ b^2sin$	$I_{YY} \propto e^2$	d'^2	s'^2	r'^2	0

When angular angle $\psi' = 0$, corresponding to the flat part (1-L) of the rolling surface, the E_{2g} Raman mode is zero for co-circular polarisation states ($\sigma^+\sigma^+$ and $\sigma^-\sigma^-$). However, for linear co-polarisation (*XX* and *YY*), a non-zero E_{2g} mode is observed. Interestingly, when the light interacts with the rolled surface at a non-zero ψ' (curved part of the surface), the E_{2g} mode becomes non-zero for both circular and linear polarisation states. This effect is demonstrated for ψ' angles of 0, 30, 60, and 90º in Table 1.

The experimental Raman measurements (Figure 3) align with these predictions, showing non-zero E_{2g} modes in the $\sigma^+\sigma^+$and $\sigma^-\sigma^-$ polarised state. This confirms that symmetry reduction occurs due to the rolling surface. Such symmetry reduction alters the Raman selection rules in localised regions, in agreement with theoretical insights from tight-binding models, where changes in the Hamiltonian and orbital angular momentum components induced by curvature play a significant role[31,32].

A similar approach was applied to estimate the behaviour of the A_{1g} mode, which displayed non-zero values for every Euler angle orientation (details in the SI, Note 1). This finding is consistent with the experimental Raman data shown in Figure 3. Similar behaviour was also observed for the C_{3v} point group, representing the 3R phase of MoS_2 (details in the SI, Note 1).

Finally, we used the estimated equations for different polarisation states during θ-angular rotation to fit the angular Raman data (Figure 5). The fitting results confirmed that the angular-dependent Raman tensor equation accurately predicted the experimental observations.

In summary, we have developed a robust rolling process for MoS_2 by employing surface hydrophobisation. The rolling initiates at the centre of the flake and gradually slows due to tearing, as confirmed through direct in situ observations. This process yields regular, topologically smooth rolls that are symmetrically positioned along the edges of the original triangular flake.

The optical properties of the resulting nanostructures were investigated using polarisation-resolved Raman and PL spectroscopy. The rolling process induces a pronounced anisotropy in MoS_2, significantly modifying both excitonic emission and Raman responses. In the rolled regions, we observe a strong enhancement in PL intensity and an increased degree of circular polarisation. This enhancement arises from cumulative scattering across multiple uncoupled layers, local field effects, and optical resonances, all of which contribute to stronger PL emission compared to flat monolayer regions.

By comparing theoretical predictions of Raman intensities for bulk 2H-MoS_2 (D_{6h} symmetry) and 3R-MoS_2 (C_{3v} symmetry) with experimental data, we demonstrate how the rolling process alters the Raman response due to variations in the incidence angle of the laser beam on the curved MoS_2 surface. The close agreement between the angular-dependent Raman tensor calculations and the measured Raman intensities further supports our interpretation.

View Article Online
DOI: 10.1039/D5NH00291E

Our findings underscore the pivotal role of rolling-induced structural and optical anisotropy in tuning the properties of MoS_2. This anisotropic behaviour not only reshapes light–matter interactions but also opens new avenues for engineering polarisation-sensitive nanophotonic devices. By harnessing these effects, our work lays the groundwork for novel optical components with tunable polarisation characteristics, with promising applications in next-generation photonic and optoelectronic technologies.

Methods

Synthesis of 1-L MoS_2: MoS_2 monolayers were synthesised on a SiO_2/Si substrate via a one-step chemical vapour deposition (CVD) method in a horizontal single-zone at atmospheric pressure. An SiO_2 (300 nm)/Si wafer was used as the substrate, which was ultrasonicated in acetone and isopropyl alcohol in water baths for 10 min each and dried using ultra-pure argon gas. The substrate was placed face-down onto a quartz crucible containing 36 mg of MoO_2 (Sigma Aldrich: LOT: STBH3472, purity 99%), and approximately 1 mg of NaCl (Sigma Aldrich: LOT: SLCC4856, purity ≥ 99%) evenly distributed. This setup was then loaded into the small quartz tube and positioned in the appropriate heating zone.

Next, 82 mg of sulfur (Thermo Scientific: LOT: T29G013, purity 99.9995%) was placed at the edge of the small quartz tube, approximately 20 cm away from the crucible. Before heating, the large quartz tube containing the small quartz tube was purged with 120 sccm argon at atmospheric pressure for 15 min. The furnace was first heated from room temperature to 800 °C at a rate of 40 °C/min to ensure a high nucleation density, keeping the sulfur portion outside furnace. Growth of MoS_2 was initiated by moving the quartz tube and introducing sulfur into furnace at approximately 750 °C for 10 min. The argon flow was maintained throughout the reaction. After growth, the furnace was allowed to cool slowly to room temperature.

Rolling of 1-L MoS_2: A mixture of deionised water and ethanol (Penta Chemical: Batch no.: 2309030920, purity 96% p.a.) in a 2:1 ratio was dropped onto the SiO_2/Si substrate containing the CVD-grown flakes. Three sample types were tested: as-prepared (fresh), naturally aged under ambient conditions, and treated by styrene (Sigma Aldrich: LOT: S054677 9345, saturation concentration in air: 25.6 g/m^3 (20 °C), purity ≥ 99%). The rolling process was captured using a CCD camera attached to an optical microscope (Olympus).

Atomic force microscopy: Atomic force microscopy (AFM) images and height (thickness) profiles were obtained using Bruker's Dimension ICON atomic force microscope system in peak force quantitative nanomechanical mapping mode with a Bruker silicon tip. The AFM data were processed and analysed by open-access Gwyddion software.

Raman and PL microspectroscopy: Preliminary unpolarised spectra and testing maps were collected in backscattering geometry with a WITec alpha300R confocal Raman microscope using an excitation wavelength of 532 nm (2.33 eV) at 300 μW power. Both types of polarised spectra and their angular dependencies were measured using an in-house spectroscopic setup. The schematic ray diagram of the spectroscopic setup is shown in SI (see Figure S14). Spectra and spectral maps were collected in the backscattering geometry using a confocal Raman microscope insert (attoRAMAN, attocube).

A 100× objective lens (numerical aperture 0.82, lateral resolution of 500 nm) was used to focus the 532 nm (2.33 eV) laser excitation of linearly and circularly polarised light at 300 μW power. The outgoing signal was captured by the WITec alpha300R spectrometer, connected to the optical setup. The spectral resolution of the spectrometer under the measurement conditions using 600/1800 lines/cm grating, was 0.5 cm^{-1}.

The incident laser beam was circularly polarised using a set of standard 532 nm half- and quarter-wave plates. Similarly, a series of broadband quarter- and half-wave plates was used to obtain polarisation-resolved emitted signals. The degree of polarisation was pre-calibrated for each incident and scattered beam using ThorLabs TXP polarimeter. The intensity response of the charge-couple device (CCD) detector was pre-calibrated using a tungsten halogen light source (HL-2000-CAL, Ocean Optics). Data were analysed using custom routines in MATLAB, where individual peaks were fitted using the pseudo-Voigt function (with the Gaussian component primarily accounting for peak parameter distribution within the laser spot).

Acknowledgements

The work was supported by the Czech Science Foundation, project no. 22-17517S and Ministry of Education, Youth and Sports of the Czech Republic, project AMULET, no. CZ.02.01.01/00/22_008/0004558.

View Article Online
DOI: 10.1039/D5NH00291E

Data Availability Statement

Data for this article are available at Zenodo (https://zenodo.org/) at https://zenodo.org/records/15106532.

Conflicts of Interest

The authors declare no conflict of interest.

References

1 K. B. Simbulan, Y.-J. Feng, W.-H. Chang, C.-I. Lu, T.-H. Lu and Y.-W. Lan, *ACS Nano*, 2021, **15**, 14822–14829.

2 K. Liu, Q. Yan, M. Chen, W. Fan, Y. Sun, J. Suh, D. Fu, S. Lee, J. Zhou, S. Tongay, J. Ji, J. B. Neaton and J. Wu, *Nano Lett*, 2014, **14**, 5097–5103.

3 C. Li, Q. Cao, F. Wang, Y. Xiao, Y. Li, J.-J. Delaunay and H. Zhu, *Chem. Soc. Rev.*, 2018, **47**, 4981–5037.

4 Y. Jiang, S. Chen, W. Zheng, B. Zheng and A. Pan, *Light Sci Appl*, 2021, **10**, 72.

5 Y. Huang, J. Guo, Y. Kang, Y. Ai and C. M. Li, *Nanoscale*, 2015, **7**, 19358–19376.

6 H. Li, H. Wu, S. Yuan and H. Qian, *Sci Rep*, 2016, **6**, 21171.

7 X. Cui, Z. Kong, E. Gao, D. Huang, Y. Hao, H. Shen, C. Di, Z. Xu, J. Zheng and D. Zhu, *Nat Commun*, 2018, **9**, 1301.

8 G. Seifert, H. Terrones, M. Terrones, G. Jungnickel and T. Frauenheim, *Phys. Rev. Lett.*, 2000, **85**, 146–149.

9 S. Aftab, M. Z. Iqbal and Y. S. Rim, *Small*, 2023, **19**, 2205418.

10 R. Ghosh, H.-I. Lin, Y.-S. Chen, M. Singh, Z.-L. Yen, S. Chiu, H.-Y. Lin, K. P. Bera, Y.-M. Liao, M. Hofmann, Y.-P. Hsieh and Y.-F. Chen, *Small*, 2020, **16**, 2003944.

11 J. M. de Albornoz-Caratozzolo and F. Cervantes-Sodi, *Nanoscale Adv.*, 2024, **6**, 79–91.

12 S. Yu, H. Ye, S. Wang, H. Tang, P. Wang, C. Pei, Y. Yang, X. Huang and H. Li, *ACS Appl Nano Mater*, 2024, **7**, 18801–18810.

13 D. Yang, L. Li, X. Wei, Y. Wang, W. Zhou, H. Kataura, S. Xie and H. Liu, *Sci Adv*, 2021, **7**, eabe0084.

14 A. Castellanos-Gomez, H. S. J. van der Zant and G. A. Steele, *Nano Res*, 2014, **7**, 572–578.

15 S. M. Shinde, K. P. Dhakal, X. Chen, W. S. Yun, J. Lee, H. Kim and J.-H. Ahn, *NPG Asia Mater*, 2018, **10**, e468–e468.

16 C. A. Bhuyan, K. K. Madapu, K. Prabakar, K. Ganesan, S. Amirthapandian and S. Dhara, *ACS Appl Nano Mater*, 2025, **8**, 8993–9003.

17 L. Wang, Q. Yue, C. Pei, H. Fan, J. Dai, X. Huang, H. Li and W. Huang, *Nano Res*, 2020, **13**, 959–966.

18 Z. Ao, C. Liu, H. Ma, X. Lan, J. Zhang, B. Zhang, F. Zhang, Z. Wang, P. Chen, M. Zhong, G. Wang and Z. Zhang, *Small*, 2024, **20**, 2404897.

19 B. Zhang, Z. Ao, X. Lan, J. Zhong, F. Zhang, S. Zhang, R. Yang, L. Wang, P. Chen, G. Wang, X. Yang, H. Liu, J. Cao, M. Zhong, H. Li and Z. Zhang, *Nano Lett*, 2024, **24**, 7716–7723.

20 J. Su, X. Li, M. Xu, J. Zhang, X. Liu, X. Zheng, Y. Shi and Q. Zhang, *ACS Appl Mater Interfaces*, 2023, **15**, 3307–3316.

21 R. Wang, S. Guo, Z. Li, D. Weller, S. Quan, J. Yu, M. Wu, J. Jiang, Y. Wang and R. Liu, *J Phys Chem Lett*, 2022, **13**, 8409–8415.

22 G. Rusciano, A. Capaccio, A. Sasso, M. Singh, M. Valadan, C. Dell'Aversana, L. Altucci and C. Altucci, *Front Bioeng Biotechnol*, 2022, **10**, 844011.

23 A. M. Shafi, F. Ahmed, H. A. Fernandez, M. G. Uddin, X. Cui, S. Das, Y. Dai, V. Khayrudinov, H. H. Yoon, L. Du, Z. Sun and H. Lipsanen, *ACS Appl Mater Interfaces*, 2022, **14**, 31140–31147.

24 M. Kaneda, W. Zhang, Z. Liu, Y. Gao, M. Maruyama, Y. Nakanishi, H. Nakajo, S. Aoki, K. Honda, T. Ogawa, K. Hashimoto, T. Endo, K. Aso, T. Chen, Y. Oshima, Y. Yamada-Takamura, Y. Takahashi, S. Okada, T. Kato and Y. Miyata, *ACS Nano*, 2024, **18**, 2772–2781.

25 J. Zhang, S. Jia, I. Kholmanov, L. Dong, D. Er, W. Chen, H. Guo, Z. Jin, V. B. Shenoy, L. Shi and J. Lou, *ACS Nano*, 2017, **11**, 8192–8198.

View Article Online
DOI: 10.1039/D5NH00291E

26 S. Wang, M. S. Ukhtary and R. Saito, *Phys. Rev. Res.*, 2020, **2**, 33340.

27 Q. Zhang, Y. Cheng, L.-Y. Gan and U. Schwingenschlögl, *Phys. Rev. B*, 2013, **88**, 245447.

28 K. F. Mak, K. He, J. Shan and T. F. Heinz, *Nat Nanotechnol*, 2012, **7**, 494–498.

29 T. Verhagen, V. L. P. Guerra, G. Haider, M. Kalbac and J. Vejpravova, *Nanoscale*, 2020, **12**, 3019–3028.

30 L. Du, T. Hasan, A. Castellanos-Gomez, G.-B. Liu, Y. Yao, C. N. Lau and Z. Sun, *Nature Reviews Physics*, 2021, **3**, 193–206.

31 A. J. Pearce, E. Mariani and G. Burkard, *Phys Rev B*, 2016, **94**, 155416.

32 Y. J. Zhang, T. Ideue, M. Onga, F. Qin, R. Suzuki, A. Zak, R. Tenne, J. H. Smet and Y. Iwasa, *Nature*, 2019, **570**, 349–353.

33 P. Král, E. J. Mele and D. Tománek, *Phys Rev Lett*, 2000, **85**, 1512–1515.

34 G. L. Frey, S. Elani, M. Homyonfer, Y. Feldman and R. Tenne, *Phys Rev B*, 1998, **57**, 6666–6671.

35 E. S. Kadantsev and P. Hawrylak, *Solid State Commun*, 2012, **152**, 909–913.

36 I. Paradisanos, S. Shree, A. George, N. Leisgang, C. Robert, K. Watanabe, T. Taniguchi, R. J. Warburton, A. Turchanin, X. Marie, I. C. Gerber and B. Urbaszek, *Nat Commun*, 2020, **11**, 2391.

37 R. Rajarapu, P. K. Barman, B. Biswal, S. Poudyal, R. Yadav, M. Deka, W. Rahman, A. S, P. K. Nayak and A. Misra, *Appl Phys Lett*, 2024, **124**, 033103.

38 S. M. Shinde, K. P. Dhakal, X. Chen, W. S. Yun, J. Lee, H. Kim and J.-H. Ahn, *NPG Asia Mater*, 2018, **10**, e468–e468.

39 R. Kesarwani, H. Chaturvedi and A. Khare, in *13th International Conference on Fiber Optics and Photonics*, Optica Publishing Group, 2016, p. P1A.18.

40 D. R. Kazanov, A. V Poshakinskiy, V. Yu. Davydov, A. N. Smirnov, I. A. Eliseyev, D. A. Kirilenko, M. Remškar, S. Fathipour, A. Mintairov, A. Seabaugh, B. Gil and T. V Shubina, *Appl Phys Lett*, 2018, **113**, 101106.

41 B. Visic, R. Dominko, M. K. Gunde, N. Hauptman, S. D. Skapin and M. Remskar, *Nanoscale Res Lett*, 2011, **6**, 593.

View Article Online
DOI: 10.1039/D5NH00291E

42 J. Huang, Z. Liu, T. Yang and Z. Zhang, *J Mater Sci Technol*, 2022, **102**, 132–136.

43 J. Huang, Z. Liu, T. Yang and Z. Zhang, *J Mater Sci Technol*, 2022, **102**, 132–136.

44 J. Ribeiro-Soares, R. M. Almeida, E. B. Barros, P. T. Araujo, M. S. Dresselhaus, L. G. Cançado and A. Jorio, *Phys Rev B*, 2014, **90**, 115438.

45 A. M. Jones, H. Yu, N. J. Ghimire, S. Wu, G. Aivazian, J. S. Ross, B. Zhao, J. Yan, D. G. Mandrus, D. Xiao, W. Yao and X. Xu, *Nat Nanotechnol*, 2013, **8**, 634–638.

46 A. N. Rudenko and M. I. Katsnelson, *2d Mater*, 2024, **11**, 042002.

47 A. Ghazaryan, M. Hafezi and P. Ghaemi, *Phys Rev B*, 2018, **97**, 245411.

48 C. Lee, H. Yan, L. E. Brus, T. F. Heinz, J. Hone and S. Ryu, *ACS Nano*, 2010, **4**, 2695–2700.

49 X. Zhang, X.-F. Qiao, W. Shi, J.-B. Wu, D.-S. Jiang and P.-H. Tan, *Chem. Soc. Rev.*, 2015, **44**, 2757–2785.

50 T.-D. Huang, K. B. Simbulan, Y.-F. Chiang, Y.-W. Lan and T.-H. Lu, *Phys Rev B*, 2019, **100**, 195414.

51 M. I. Aroyo, A. Kirov, C. Capillas, J. M. Perez-Mato and H. Wondratschek, *Acta Crystallographica Section A*, 2006, **62**, 115–128.

52 M. I. Aroyo, J. M. Perez-Mato, C. Capillas, E. Kroumova, S. Ivantchev, G. Madariaga, A. Kirov and H. Wondratschek, 2006, **221**, 15–27.

53 M. I. Aroyo, J. M. Perez-Mato, D. Orobengoa, E. Tasci, G. de la Flor and A. Kirov, *Bulg. Chem. Commun*, 2011, **43**, 183–197.

View Article Online
DOI: 10.1039/D5NH00291E

Figures

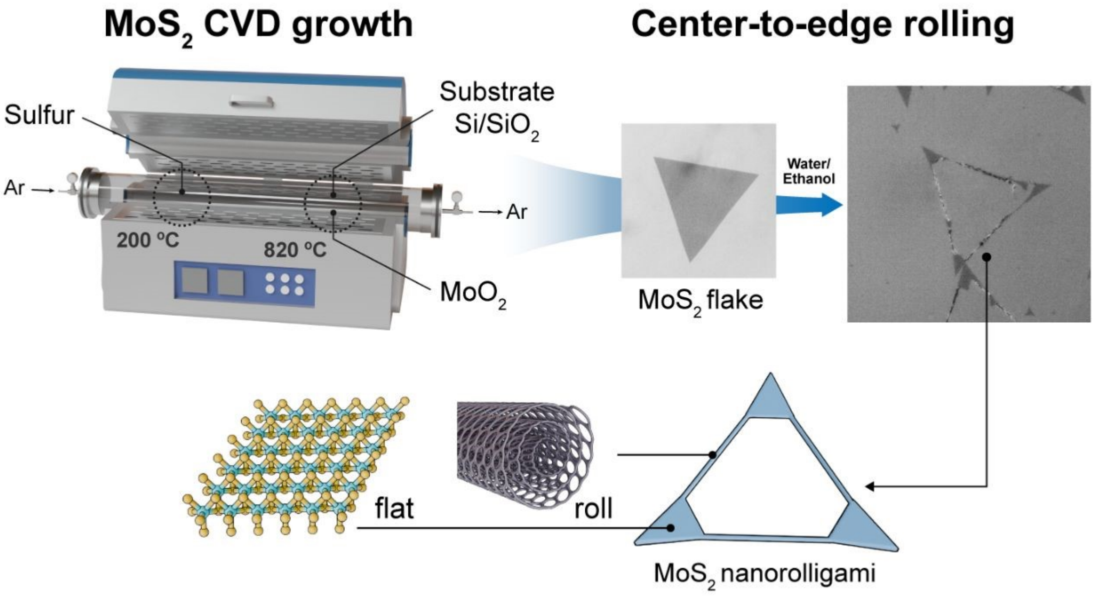

Figure 1: Step-by-step description of the nanorollingami process. In the first step, the monolayer (1-L) MoS_2 is prepared via the CVD technique. The second step is to roll the 1-L MoS_2 by dripping a solution of water and ethanol in a 2:1 ratio at room temperature (RT). The solution causes a strong mechanical strain in the central part of the 1-L MoS_2, resulting in a break from the center and self-rolling at each corner. The in-situ video of self-rolling MoS_2 has been recorded using a microscope.

View Article Online
DOI: 10.1039/D5NH00291E

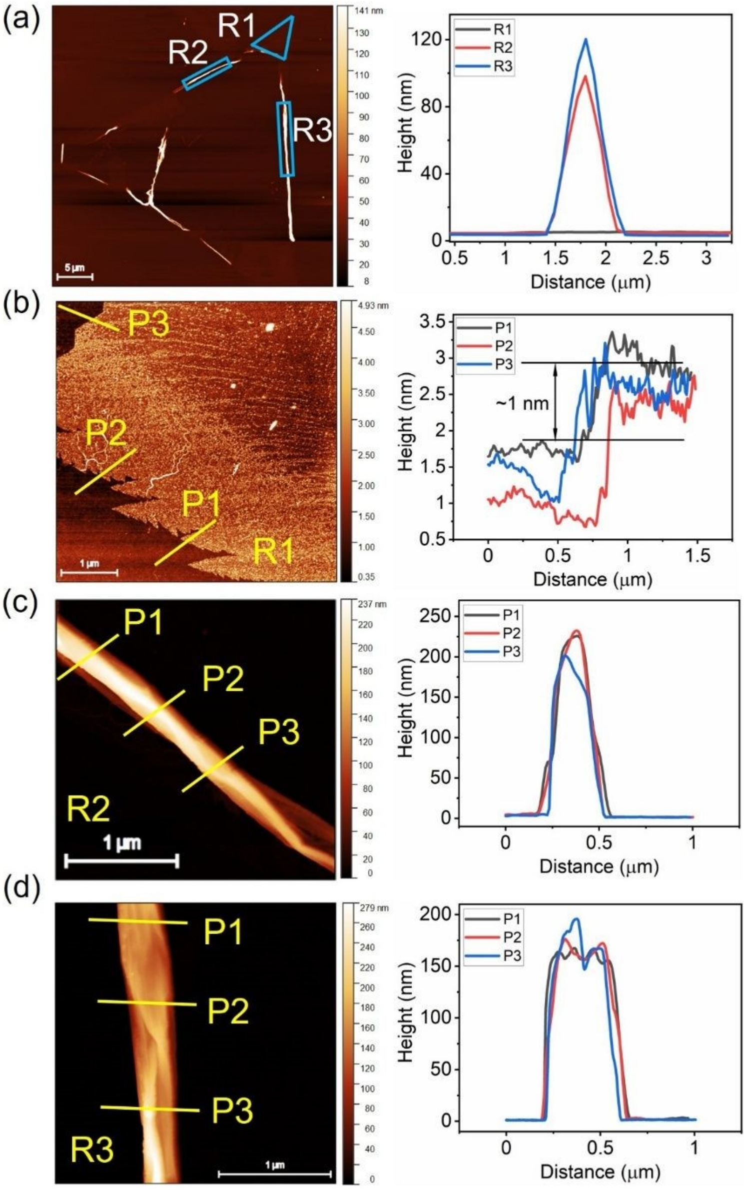

Figure 2: Surface morphology of nanorollingami. The comparative thickness between flat and rolling regions (represented by R) is analyzed through AFM. (a) The nanorollingami film shows three marked regions: flat and two rolling. The height profile from line scans at specific points in these regions is plotted on the right side for comparison. Enlarged scans of each region are provided for a clear understanding of their surface morphology. (b) The first flat region corresponds to 1-L MoS_2, as confirmed by thickness measurements taken at three different positions within this region, shown on the right, clearly indicating the monolayer structure. (c)

The second region features rolling MoS_2. Distinct rolling forms are observed at different marked positions, each showing varying thicknesses. (d) The third region also consists of rolled MoS_2 but exhibits a nearly uniform rolling pattern, as evidenced by consistent thickness measurements at all marked positions on the right side.

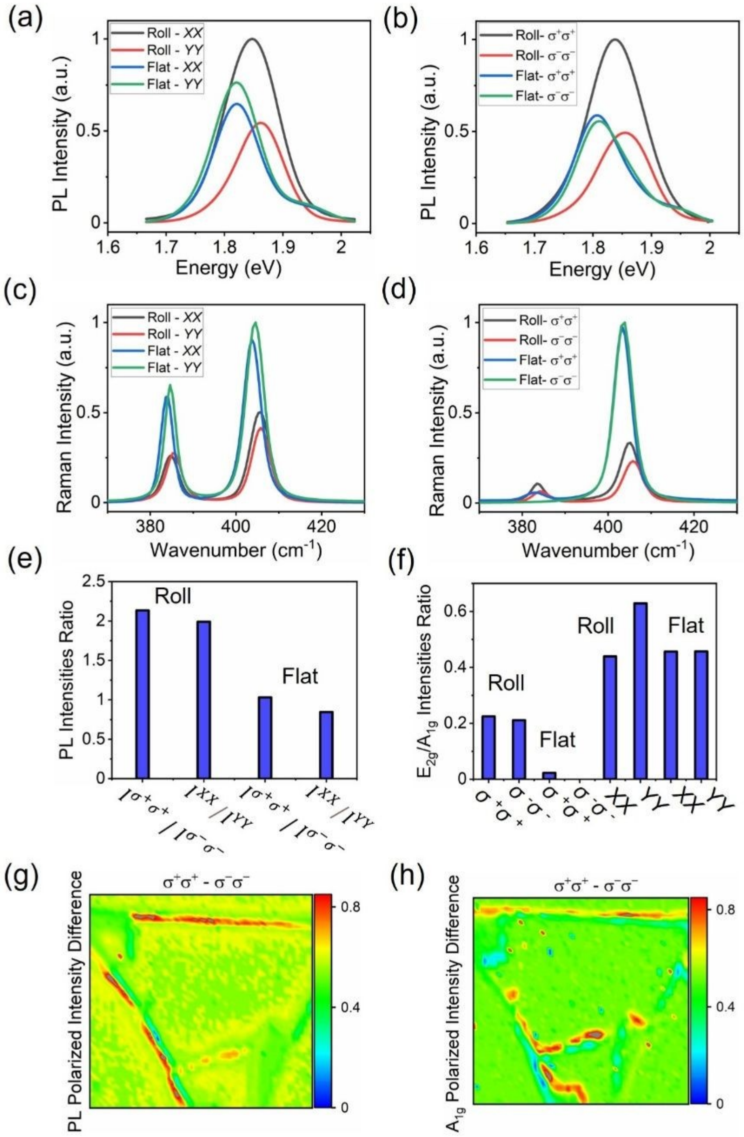

Figure 3: Optical characterization of nanorollingami. The PL and Raman characterization of the nanorollingami at RT under excitation (in) and detection (out) of four polarized light measurements combinations: horizontally-in and horizontally-out (called *XX*), vertically-in and vertically-out (called *YY*), right circular-in and right circular-out (called $\sigma^+\sigma^+$), and left circular-in and left circular-out (called $\sigma^-\sigma^-$). (a) and (b) show the normalized PL intensity, (c) and (d) depict the normalized Raman intensity of rolled and flat regions for the set of linear (*XX* and *YY*) and circularly ($\sigma^+\sigma^+$ and $\sigma^-\sigma^-$) polarized light, respectively. (e) compares the PL integral intensity ratio of "$\sigma^+\sigma^+$" and "$\sigma^-\sigma^-$" light and "*XX*" and "*YY*" polarized light at both

View Article Online
DOI: 10.1039/D5NH00291E

rolled and flat regions. (f) compares the integral intensity ratio of E$_{2g}$ (~ 384 cm^{-1}) and A$_{1g}$ (~ 404 cm^{-1}) Raman modes at all sets of polarized lights for both rolled and flat regions. (g) and (h) illustrate the difference in the normalized intensities of PL ($\sigma^+\sigma^+$ and $\sigma^-\sigma^-$-polarized states) and the A$_{1g}$-mode of Raman, respectively.

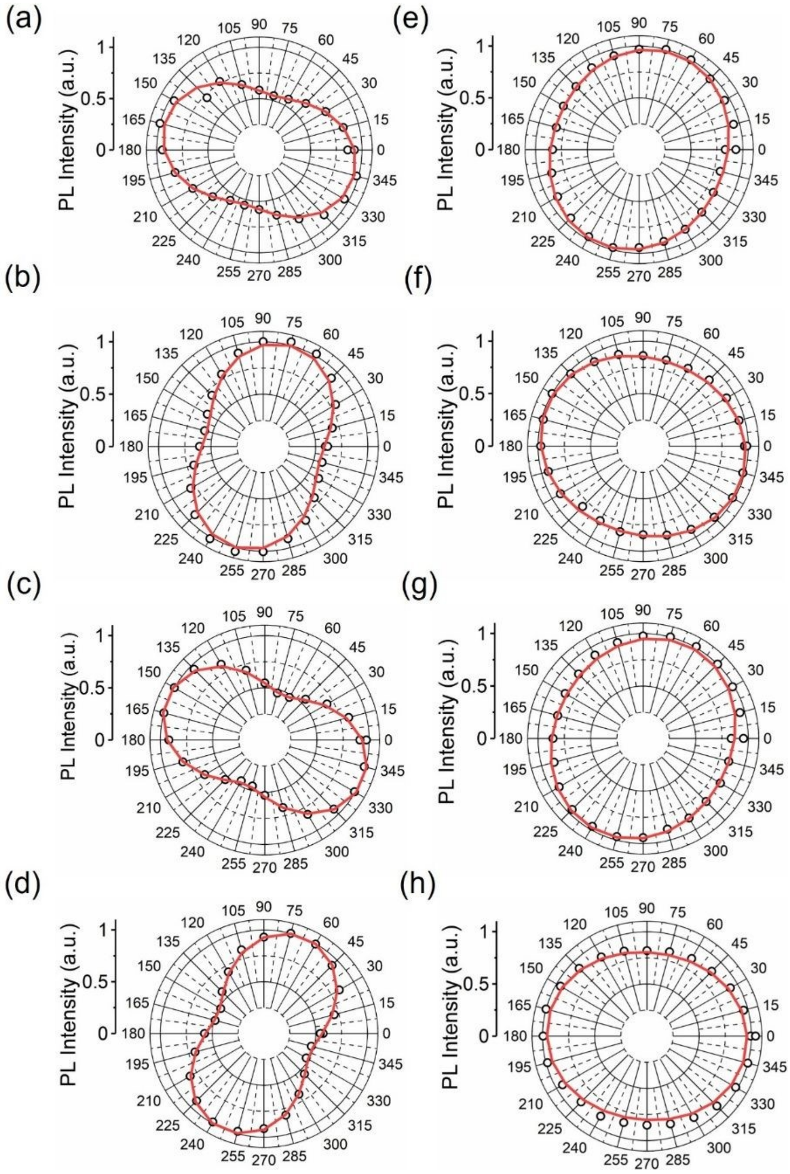

Figure 4: PL angular characterization of nanorollingami. Angular characterization is performed by varying the analyzer angles from 0° to 360° at 15° intervals to fix the plane of incident polarized light at RT. The circles correspond to the measured data, while the solid red line represents the fitting (equation shown below in text). (a) to (d) show the angular normalized PL intensity for the rolled region, and (e) to (h) show the angular normalized PL intensity for

View Article Online
DOI: 10.1039/D5NH00291E

the flat region, each excited by horizontal (*X*), vertical (*Y*), right circular (σ^+), and left circular (σ^-) polarized light, respectively.

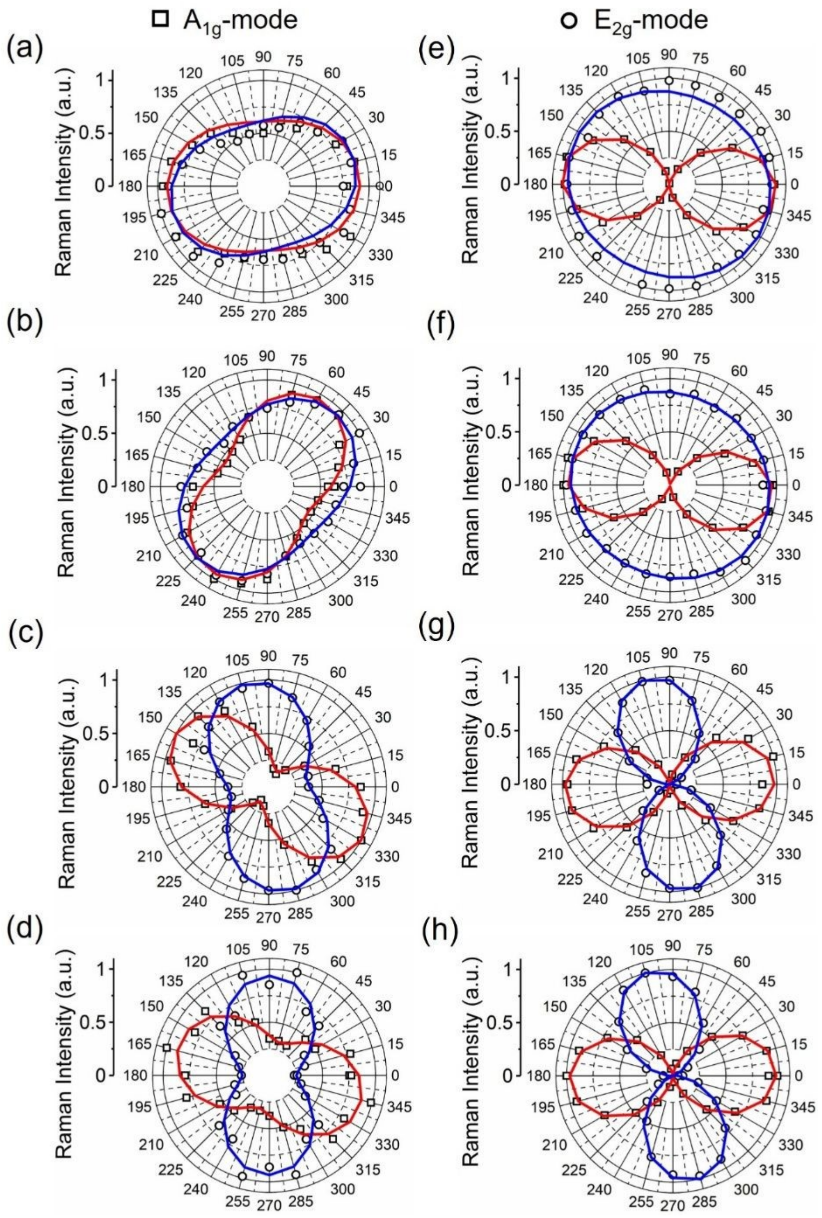

Figure 5: Raman angular characterization of nanorollingami. Angular measurements are performed similarly to the PL characterization. Square and circles correspond to the measured data of A_{1g} and E_{2g} modes, respectively, while the solid red and blue lines represent the fitting (equation shown in SI). (a) to (d) show the angular normalized Raman intensity for the rolling

View Article Online
DOI: 10.1039/D5NH00291E

region, and (e) to (h) depicts the angular normalized Raman intensity for the flat region, each excited by horizontal (*X*), vertical (*Y*), right circular (σ^+), and left circular (σ^-) polarized light, respectively.

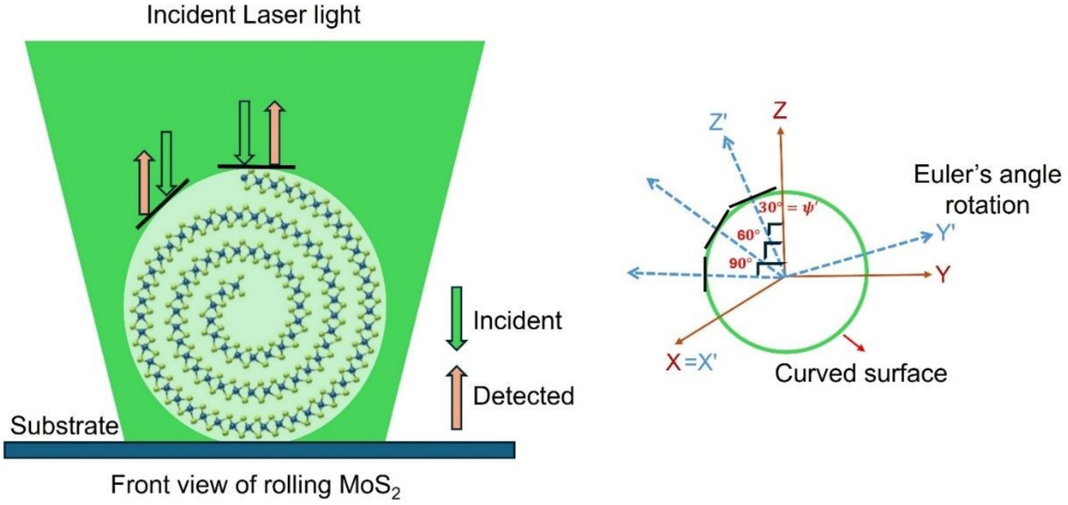

Figure 6: Illustration of laser interaction with rolled surface. Schematic representation of the interaction between a horizontally polarized laser beam and a rolling surface of MoS_2, illustrating how changes in the Euler angle (ψ') occur as the beam interacts with different curved regions of the rolling surface. This setup demonstrates the variation in light incidence across the rolling surface.

View Article Online
DOI: 10.1039/D5NH00291E

Data availability statement

The data supporting the findings of this study are available within the article and its supplementary information files. Additional data sets are available at Zenodo (https://zenodo.org/) at https://zenodo.org/records/15106532.